Electronic Supplementary Material (ESI) for Faraday Discussions.

Supplementary Information for 'Singlet Fission is Incoherent in Pristine Orthorhombic Single Crystals of Rubrene: No Evidence of Triplet-Pair Emission'

David G. Bossanyi, Rahul Jayaprakash, and J. Clark

Department of Physics and Astronomy, University of Sheffield, Hounsfield Road, Sheffield S3 7RH, UK

Maik Matthiesen and Jana Zaumseil

Institute for Physical Chemistry, Heidelberg University, Heidelberg, Germany

Sayantan Bhattacharya

Department of Life Sciences, Imperial College, London SW15 4JD, UK

(Dated: September 22, 2023)

Contents

1. Methods

1.1 Sample preparation

Rubrene single crystal growth and thin film fabrication are described below.

1.1.1 Rubrene single crystal growth

Rubrene for single crystal growth was purchased from Merck and grown using physical vapour transport. Single crystals of organic semiconductors can be readily grown by physical vapour transport (PVT) [1, 2]. A small quantity of starting material is placed in the hottest part of a horizontal tube furnace, along which a slow, steady flow of carrier gas is flowing. The starting material sublimes and molecules are transported by the carrier gas down the tube furnace, along which a negative temperature gradient is applied. Once molecules reach a cooler region of the furnace, they can attach themselves to the crystals forming there. Impurities generally crystallise at a different temperature to the target molecule, thus they are spatially separated out by the physical vapour transport method. To obtain highly pure crystals, the sublimation is repeated a second time, using crystals grown during the first growth run as the starting material.

A horizontal PVT furnace (Trans Temp, Thermcraft) was used for the growth, and the apparatus was enclosed to prevent possible photo-degradation.

Quartz tubes used inside the PVT furnace were first cleaned with soap and a succession of solvents before being baked at 325 °C for 16 h and allowed to cool fully. 79 mg of starting material was placed at the end of the furnace and the whole assembly was purged under flowing ultra high purity argon gas (99.999%, 50 $cm^3\,min^{-1}$) for 21 h. This gas flow was then maintained for the entirety of the first sublimation. The temperature of the starting material was next raised to 137 °C for 2.5 h and finally set at 289 °C and left for 3 d before being allowed to cool to room temperature.

Figure S1 shows the spatial separation of impurities following the first sublimation run in the PVT furnace. Figure S2 shows which of the rubrene crystals obtained from the first run were used as starting materials for the second run, and indicates the crystals used for lamination.

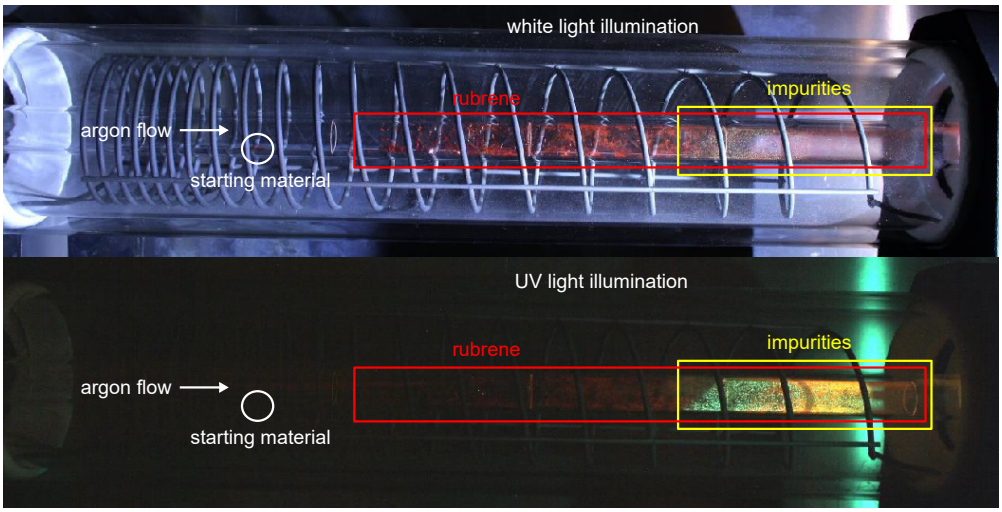

FIG. S1. **Rubrene single crystal growth I.** Photographs of the PVT furnace after the first sublimation run of rubrene. Lateral separation of impurities in the commercial starting material can be clearly observed, allowing high purity crystals to be grown in a second run.

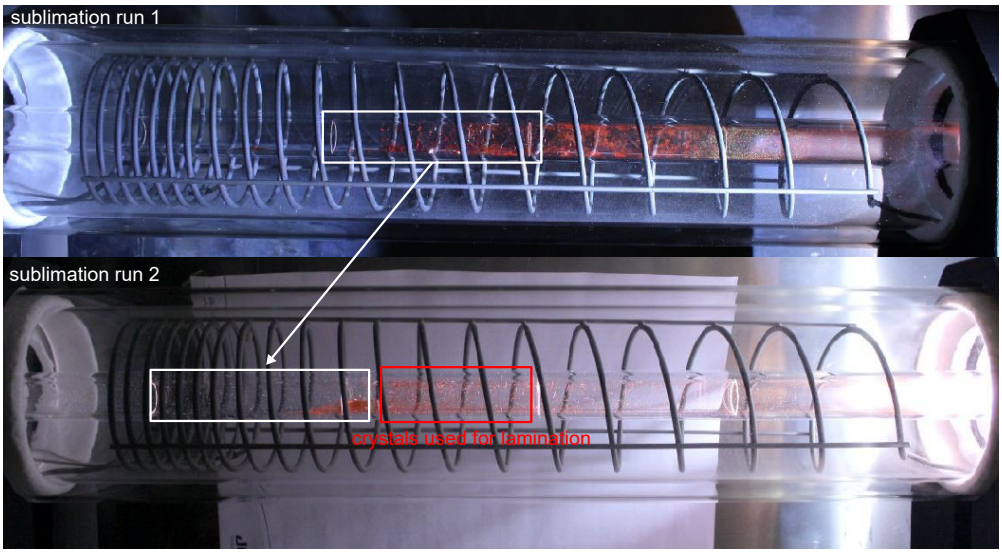

FIG. S2. **Rubrene single crystal growth II.** Photographs of the PVT furnace after the first and second sublimation runs, indicating the crystals from the first run that were used as starting material for the second. The crystals used for lamination are also highlighted.

1.1.2 Evaporated rubrene films

Rubrene powder from Ossila was placed in a ceramic crucible inside an evaporation chamber evacuated to 2×10^{-6} mbar or lower. The powder was heated to around 180 °C, causing

the rubrene to sublime and deposit itself on substrates held at the top of the chamber. The evaporation rate was continuously measured by a quartz crystal microbalance and maintained at 0.3 Å s^{-1} during deposition by PID feedback control. 125 nm of rubrene was deposited in this way. The films were then annealed at 185 °C for 17 minutes, resulting in visible spherulite formation.

1.2 Spectroscopy

1.2.1 Single crystal ground state absorption spectroscopy

Ground state absorption spectra were recorded using the probe beam of the picosecond transient absorption setup described below. The probe spot size is less than 100 µm in diameter at the sample position which is less than the smallest dimension of crystal 1 (Main text Figure 2). The transmission of the probe light was recorded through both the crystal and bare substrate (by translating the crystal laterally out of the beam focus) and the absorbance calculated from these two measurements.

1.2.2 Time-resolved photoluminescence spectroscopy

Narrowband 500 nm pump pulses were produced in a home-built non-collinear optical parametric amplifier (NOPA), seeded by a Ti:sapphire regenerative amplifier (Solstice, Spectra-Physics, 800 nm, 90 fs FWHM, 1 kHz, 4 mJ). The NOPA produces broadband pulses spanning the range 500–700 nm; the narrowband pulses were obtained by passing the NOPA output through a 500 nm bandpass filter (FWHM 10 nm). The excitation was focussed onto the sample at a 45° incidence angle by an aspheric lens (f = 32 mm). The photoluminescence was collected by the same lens (reflection geometry) at normal incidence and recorded by the spectrograph and iCCD, see Section 1.2.2a below. Filters were used to eliminate pump scatter (longpass Schott OG550 for 500 nm excitation and 532 nm notch for 532 nm excitation). The pump polarisation was set parallel to the b-axis for crystal 1. For measurements of PL anisotropy, a rotatable linear polariser was placed before the spectrograph slit. The TRPL setup is illustrated in Figure S7a.

We note that following the laboratory closure during the COVID-19 pandemic, the wavelength calibration of our spectrograph became slightly off. The measurements presented here were recorded after the laboratory reopened, but before the calibration issue was realised.

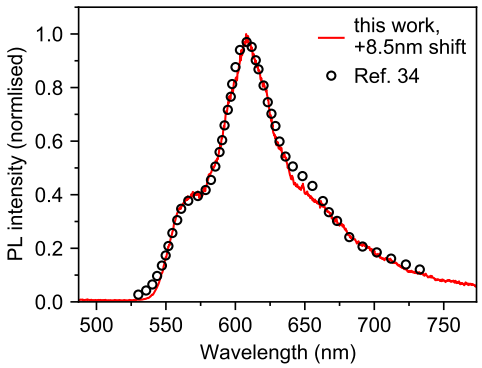

FIG. S3. **Wavelength miscalibration and comparison with literature spectra.** Normalised PL spectrum of crystal 1 (0–2 µs), recorded using our spectrograph and iCCD. The spectrum has been shifted by 8.5 nm to account for the wavelength miscalibration that occurred during a prolonged laboratory closure prior to the measurements in this chapter being taken. Our corrected spectrum closely matches an equivalent spectrum from Ref. 3, demonstrating that the 8.5 nm shift is sufficient to correct the miscalibration. Data shown by black circles adapted with permission from Reference 3; Copyright 2012 by the American Physical Society.

Therefore, all spectra presented in this paper have been shifted by 8.5 nm to correct for the miscalibration. In Figure S3, we compare such a corrected spectrum (crystal 1, 0–2 µs) against a spectrum from Ref. 3 measured for a pristine rubrene crystal under similar experimental conditions. We find that the 8.5 nm shift correction results in an extremely close match between our spectrum and the literature reference. The slight suppression of the blue edge of the spectrum in our measurement can be attributed to absorption by the 550 nm longpass filter used and the small differences around 650 nm may arise from the different crystals studied, as discussed above.

a iCCD measurements

The TRPL was recorded using an electronically-gated intensified CCD, or iCCD (iStar DH334T-18U-73, Andor) connected to a spectrograph (Shamrock 303i, Andor) that disperses the light onto the iCCD pixel array. Inside the iCCD camera, the dispersed photons are incident on a photocathode, producing photoelectrons. The photoelectrons are drawn towards a thin plate comprising a honeycomb network of small glass tubes with a resistive coating. A high potential difference is applied across this plate, which causes the photo-

electrons to accelerate and dislodge secondary electrons from the tube walls, resulting in a gain (or intensification) that depends on the applied voltage. The cloud of electrons exiting the plate next hits a phosphor screen, producing photons that are detected by a CCD array cooled to −30 °C by a Peltier element.

In addition to the extremely high sensitivity of the iCCD, the image intensifier can also act as a fast optical switch. Application of a high negative voltage between the photocathode and honeycomb plate causes the photoelectrons to be swept across the gap and subsequently detected: the iCCD is gated 'on'. If a positive voltage is applied instead, the photoelectrons are unable to cross the gap and the iCCD is gated 'off'.

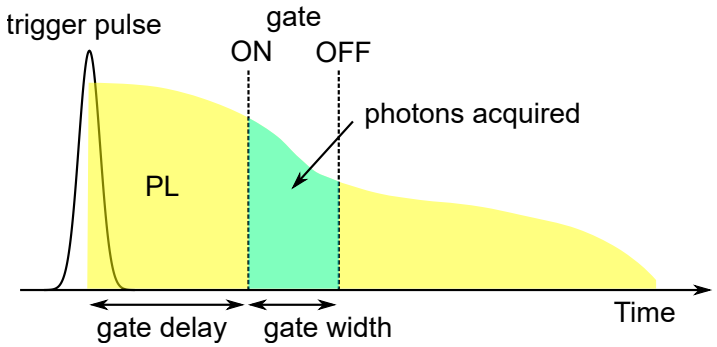

FIG. S4. **iCCD gating.** A camera read cycle is triggered for each laser shot. The gate is opened after an adjustable gate delay, remains open for an adjustable gate width and then closes. Photons are acquired by the camera during this time. Typically thousands of laser shots are averaged for each PL spectrum acquired in this way.

The timing of the electronic gating is controlled by a digital delay generator (DDG). A read cycle is initiated by an electronic trigger pulse corresponding to a pump laser shot. The DDG introduces a time delay (the 'gate delay') following receipt of the trigger, after which the iCCD is gated 'on' for a period of time called the 'gate width'. During this interval, photons are accumulated by the camera. Both the gate delay and gate width, as well as the gain voltage, can be controlled externally by computer software. In this way, photoluminescence spectra can be recorded at different time delays relative to optical excitation. This is illustrated in Figure S4. The repetition rate of the pump lasers used was either 1 kHz or 5 kHz and each spectrum is an average of many hundreds of laser shots. The shortest possible gate width is principally determined by the photocathode and gating electronics

and is around 2 ns for our system. The longest gate delay depends on the repetition rate of the laser; for example it is 1 ms for a 1 kHz repetition rate.

In order to measure the dynamics of the PL as a function of time, the gate delay is incremented by a gate step for each data point. Since the PL signal decreases with time as the excited states decay, the signal to noise ratio gets progressively worse at later time delays. To overcome this and take advantage of the excellent sensitivity of the iCCD over the full range of timescales that we can measure (ns to ms), the PL dynamics were recorded in short sections, using a constant gate step and gate width for each section (Figure S5a). The gate width was always less than or equal to the gate step. The gate delay, width and step were increased for each subsequent section. The gain and exposure (number of shots accumulated) could also be increased. A temporal overlap was ensured between the end of each section and the start of the following one. Background spectra were also collected for each section.

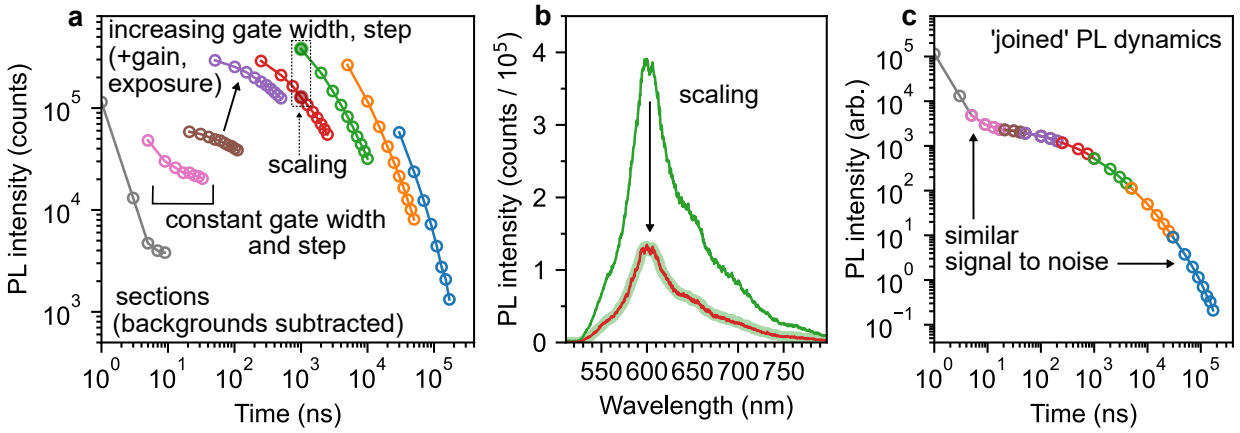

FIG. S5. **iCCD data processing.** **a**, PL dynamics are collected in sections during which the gate width and step are kept constant (shown here for $\lambda = 600$ nm). For sections starting at later time delays, the gate width and step are increased (gain and exposure can also be increased). **b**, At the overlapping time point between sections, the second PL spectrum is scaled by a constant factor such that it coincides with the first. **c**, This procedure results in a complete TRPL dataset (plotted here for $\lambda = 600$ nm).

To obtain the full TRPL dynamics, the sections were joined together. First, the background was subtracted from every spectrum in each section. Next, at each overlapping time point between sections, the second section was scaled by a constant factor until the spectra

at the overlapping time point exactly match in shape and intensity. In this way, the true PL kinetics can be obtained over many orders of magnitude in time and intensity whilst maintaining a good signal to noise ratio. This procedure for obtaining complete TRPL dynamics using the iCCD is illustrated in Figure S5.

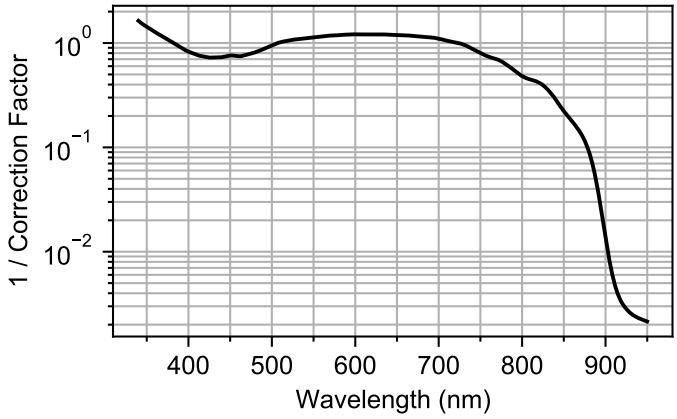

FIG. S6. **iCCD spectral sensitivity.** Spectral sensitivity of our iCCD measured by Andrew Musser using a calibrated light source. The sensitivity is flat in the visible spectral region but drops off significantly in the near-infrared.

The spectral sensitivity of our iCCD is governed principally by the photocathode (third generation 'VIH') and spectrograph grating (blazed at 500 nm, 150 lines per mm). Figure S6 shows the spectral sensitivity of our iCCD, measured by Andrew Musser using a calibrated broadband light source. The sensitivity is almost constant across the visible spectral region, but decreases significantly in the near-infrared. All PL spectra recorded using the iCCD and presented here have been corrected for spectral sensitivity.

The optical setup surrounding our iCCD is highly configurable and was adjusted and optimised based on the sample and type of measurement. Figure S7 shows the most common configurations. Figure S7a shows the standard configuration used for the measurements reported in this paper. Figure S7b illustrates how the setup can be modified to allow a magnetic field to be applied across the sample. Figure S7c shows how the sample can be placed inside a nitrogen bath cryostat, allowing TRPL data to be collected at temperatures down to 77 K.

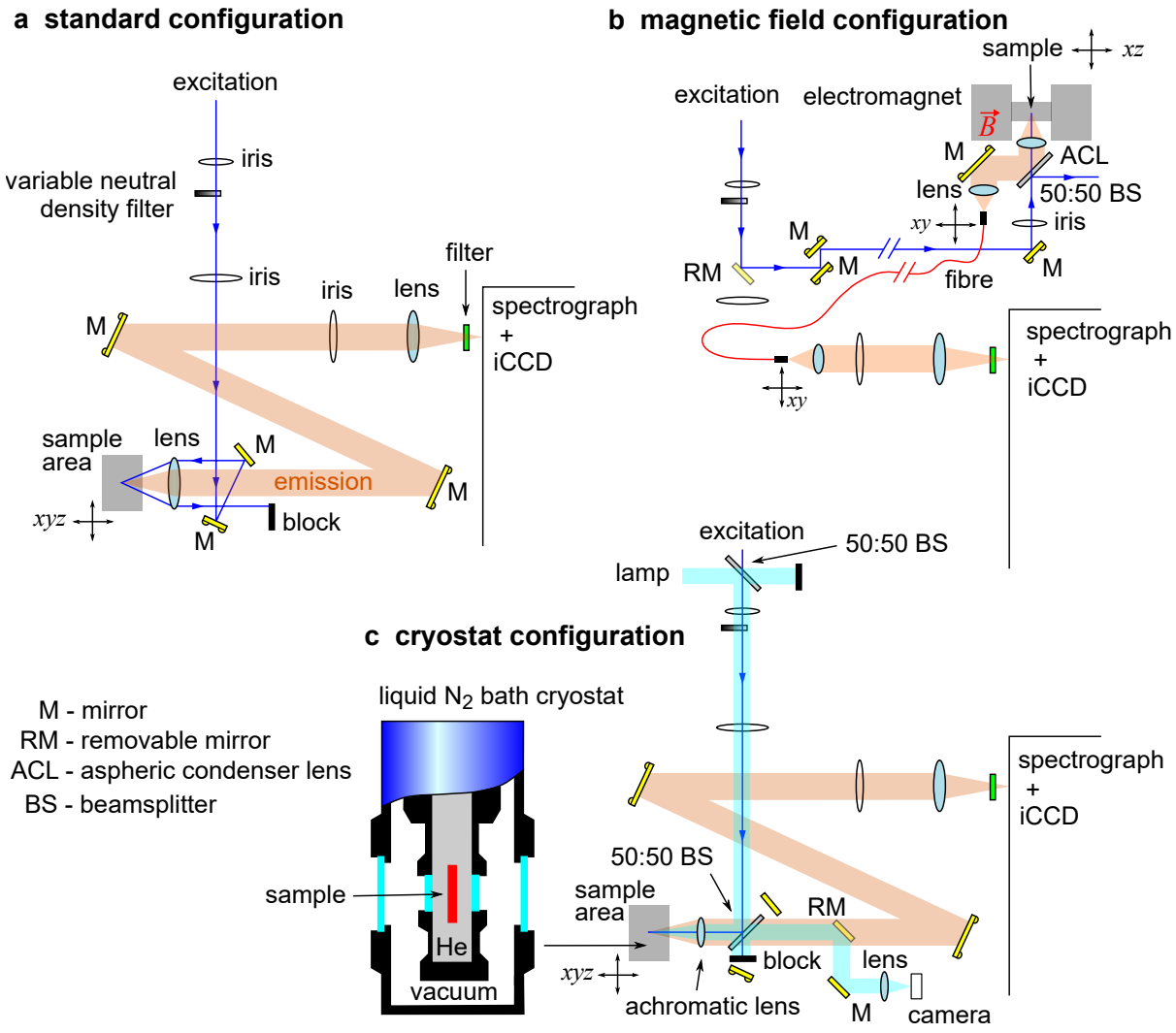

FIG. S7. **iCCD setups.** **a**, Pulsed excitation (various sources) is focussed onto the sample, usually using an aspherical condensing lens. The photoluminescence is collimated by the same lens and directed onto the entrance slit of the spectrograph. A filter is placed before the slit to remove scattered pump light. **b**, The setup can be modified to allow measurements of TRPL under applied magnetic field. Here, the PL is sent via optical fibre back to the spectrograph. **c**, The setup can also be modified to include a sample-in-exchange-gas nitrogen bath cryostat. Excitation is changed to normal incidence, which allows the sample to be simultaneously imaged using a broadband lamp and camera. This imaging capability was used to locate single crystals.

1.2.3 Transient absorption spectroscopy

We used a picosecond TA setup that is a modified version of a commercial instrument (Helios Fire, Ultrafast Systems), depicted in Figure S8. It allows transient absorption data to be collected from < 1 ps to around 7 ns in time, with a time resolution of around 100 fs.

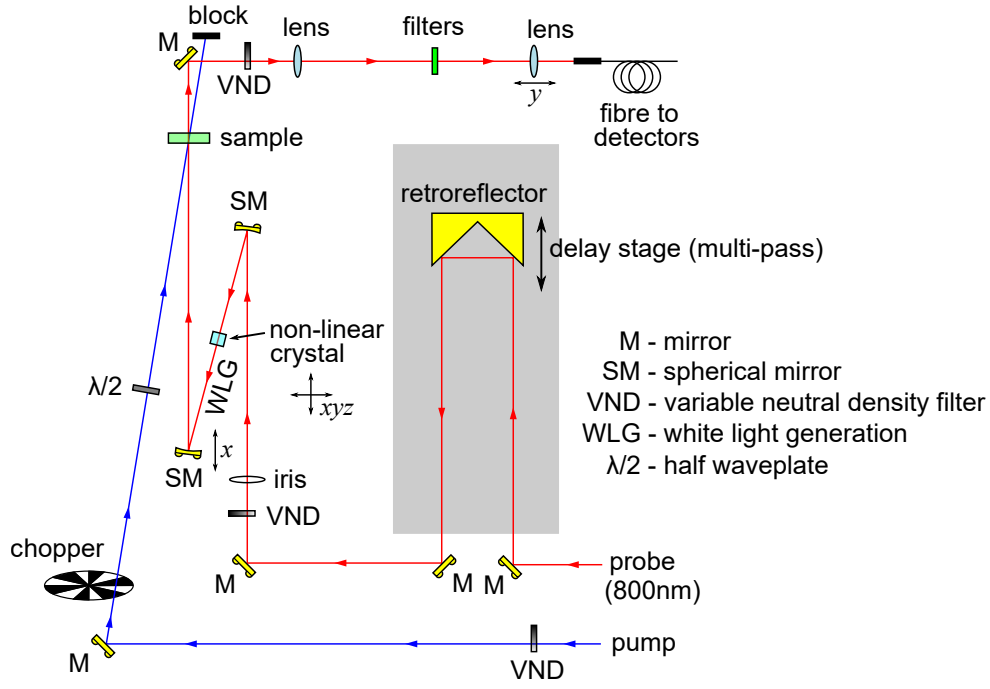

FIG. S8. **Picosecond transient absorption setup.** The probe pulses are generated by focussing the 800 nm beam through a non-linear crystal (continuously translating calcium fluoride for UV-visible or sapphire for near-infrared). The probe is focussed and overlapped with the pump (chopped to half the probe frequency) at the sample. The pump is focussed by a long focal length spherical mirror not shown in the diagram. Pump-probe delay is controlled using a motorised linear stage. Pump-probe polarisation is set using a half waveplate in the pump line.

A Ti:sapphire regenerative amplifier (Spitfire ACE PA-40, Spectra-Physics) providing 800 nm pulses (40 fs FWHM, 10 kHz, 1.2 mJ) is used to generate both the pump and probe beams. A portion of the amplifier output is passed into an optical parametric amplifier (TOPAS Prime, Light Conversion), generating tuneable narrowband pump pulses. Probe pulses spanning the ranges 350–700 nm and 850–1300 nm are generated by focussing another portion of the 800 nm beam through a continuously translating calcium fluoride or sapphire

crystal, respectively. The delay between pump and probe is controlled using a multi-pass motorized linear stage. Detection of the probe is carried out using a commercial instrument (Helios, Ultrafast Systems) equipped with CMOS and InGaAs detectors for the UV-visible and NIR spectral regions respectively.

The chirp of the probe pulses was corrected for by measuring the coherent artefact of a bare substrate. Experiments were performed with the pump polarisation both parallel and perpendicular to the probe polarisation, allowing both the isotropic signal and anisotropy (see Equation 1) to be obtained [4, 5]. Unless otherwise stated, the data presented in the paper used magic angle ($\theta = 54.7°$) configuration for the polycrystalline samples and parallel configuration for the single crystals; we show in Figure S16 that these data are proportional to the isotropic signal (in other words, the anisotropy has no time dependence).

Time-dependent anisotropy $r(t)$ is defined as

$$r(t) = \frac{\Delta A_{\parallel}(t) - \Delta A_{\perp}(t)}{\Delta A_{\parallel}(t) + 2\Delta A_{\perp}(t)} \tag{1}$$

where $\Delta A_{\parallel}(t)$ and $\Delta A_{\perp}(t)$ are measured with pump and probe polarisations parallel and perpendicular respectively.

2. Supplementary Figures and Notes

2.1 Complete transient absorption datasets

Figures S9-S13 display the complete transient absorption datasets for crystals 1 and 2 and the polycrystalline film.

2.2 510 nm probe wavelength for triplet-pair population

Figure S14 demonstrates that the transient absorption data, shown for crystal 1 with 532 nm excitation and at 30° incidence, in Figure S14a can be faithfully reproduced by an MCR-ALS [6, 7] reconstruction containing a singlet and triplet spectral component (Figure S14b). The residuals are well below 5% except in the vicinity of time-zero and the pump scatter (Figure S14c). Figure S14d shows that the kinetics at a probe wavelength of 510 nm closely match the triplet population dynamics extracted via MCR-ALS. This indicates that the kinetics at 510 nm are uncontaminated by spectral overlap from the singlet excited state

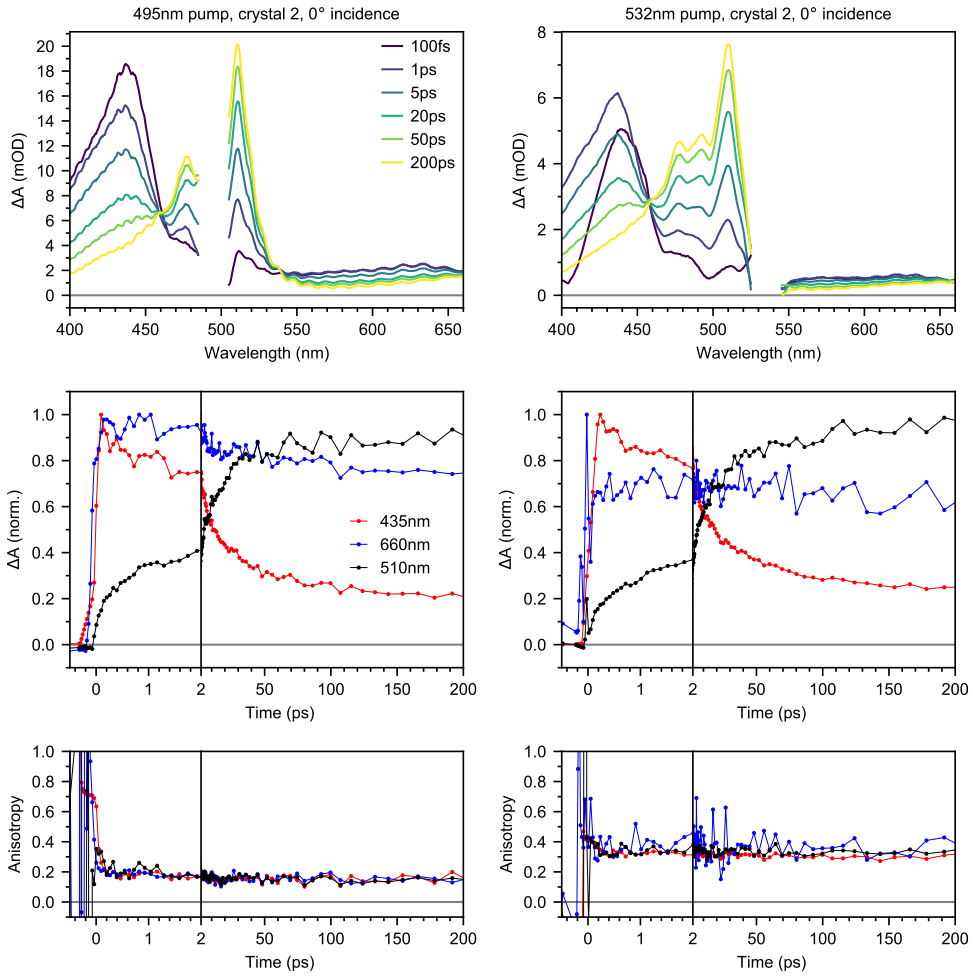

FIG. S9. **TA datasets for crystal 1, 0° incidence.** Transient absorption of crystal 1 at 0° incidence, excited with 495 nm and 532 nm pumps (left and right columns respectively). Spectra (top row) show a clear evolution from singlets ($S_1 \rightarrow S_3$ excited state absorption at 435 nm) to triplet-pairs ($T_1 \rightarrow T_3$ excited state absorption at 510 nm). The conversion is approximately one-to-one, evidenced by the isosbestic point at 460 nm. The dynamics (middle row) and anisotropy (bottom row) are shown for probe wavelengths of 435 nm (mostly singlets, some triplets), 660 nm (mixture of singlets and triplets) and 510 nm (almost entirely triplets).

absorption. The same is not true of the kinetics at 435 nm, which contain both singlet and triplet contributions.

Figure S15 shows a repeat of the MCR-ALS analysis for the polycrystalline film excited at 532 nm. Again, a good reconstruction is obtained by MCR-ALS. There is more spectral overlap between the singlet and triplet excited state absorption spectra (Figure S15b) at

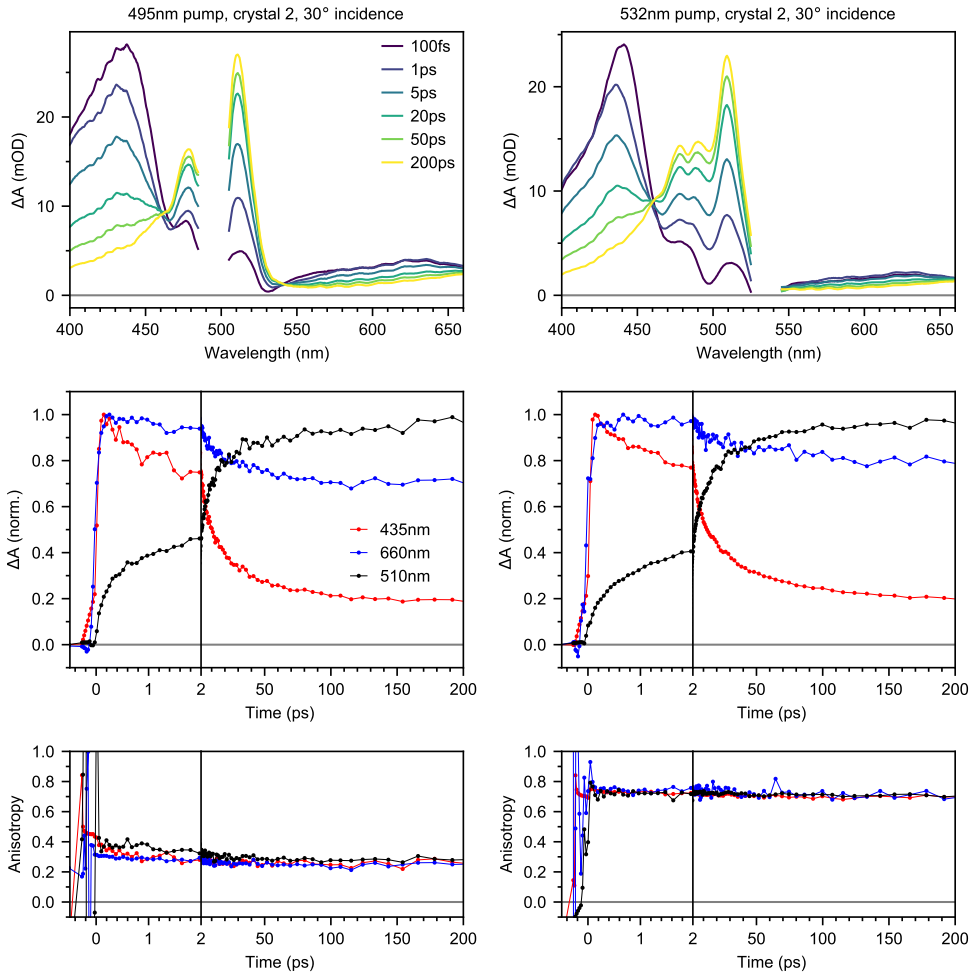

FIG. S10. **TA datasets for crystal 1, 30° incidence.** Transient absorption of crystal 1 at 30° incidence, excited with 495 nm and 532 nm pumps (left and right columns respectively). Spectra (top row) show a clear evolution from singlets ($S_1 \rightarrow S_3$ excited state absorption at 435 nm) to triplet-pairs ($T_1 \rightarrow T_3$ excited state absorption at 510 nm). The conversion is approximately one-to-one, evidenced by the isosbestic point at 460 nm. The dynamics (middle row) and anisotropy (bottom row) are shown for probe wavelengths of 435 nm (mostly singlets, some triplets), 660 nm (mixture of singlets and triplets) and 510 nm (almost entirely triplets).

510 nm due to the increased ground state bleach in the film as compared to the crystals. As a result, the match between kinetics at a probe wavelength of 510 nm and the true triplet population dynamics is not quite as close as for the crystal. Crucially however, we find that the instantaneous formation of ^{1}(TT) observed at 510 nm does not arise from spectral overlap with the S_1 signal.

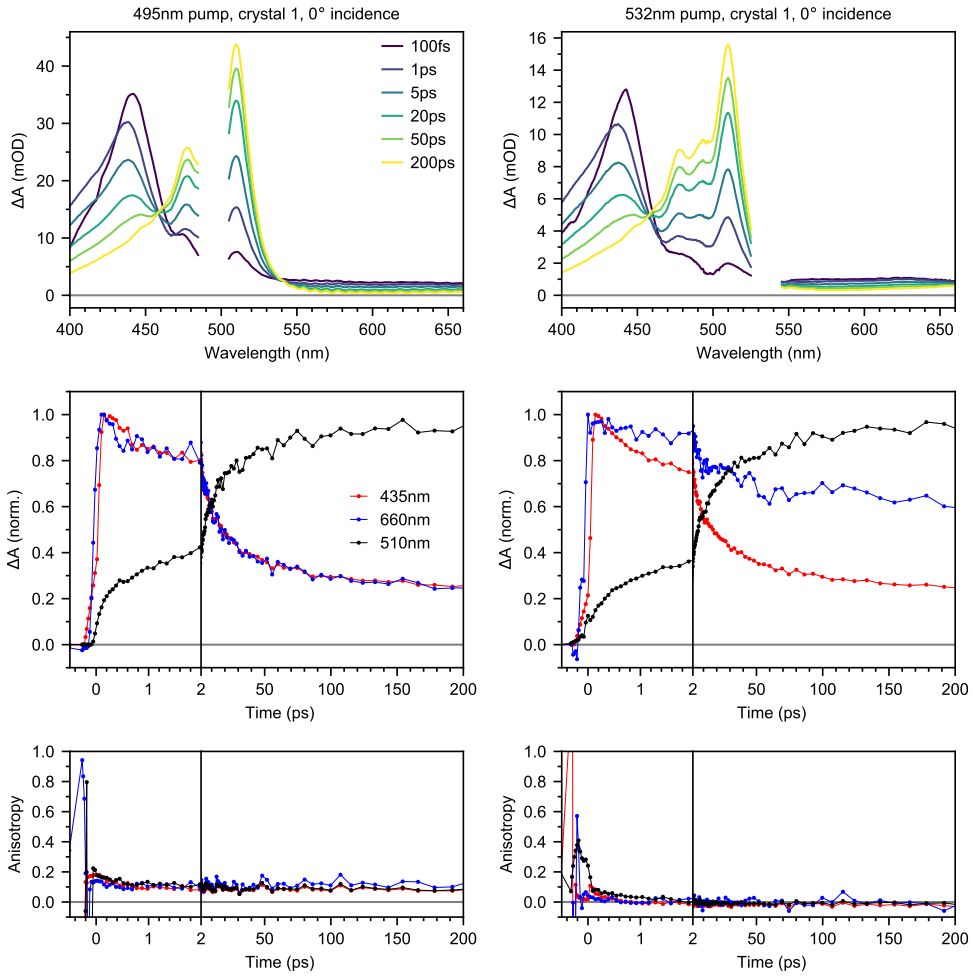

FIG. S11. **TA datasets for crystal 2, 0° incidence.** Transient absorption of crystal 2 at 0° incidence, excited with 495 nm and 532 nm pumps (left and right columns respectively). Spectra (top row) show a clear evolution from singlets ($S_1 \rightarrow S_3$ excited state absorption at 435 nm) to triplet-pairs ($T_1 \rightarrow T_3$ excited state absorption at 510 nm). The isosbestic point at 460 nm is slightly less pronounced than in crystal 1. The dynamics (middle row) and anisotropy (bottom row) are shown for probe wavelengths of 435 nm (mostly singlets, some triplets), 660 nm (mixture of singlets and triplets) and 510 nm (almost entirely triplets).

2.3 TA anisotropy

Figure S16a,b shows a comparison between the parallel and isotropic TA kinetics for crystal 1 and the polycrystalline film. The parallel data, $\Delta A_{\parallel}$, was recorded with the pump and probe polarisations parallel. Data was also recorded with pump and probe polarisations

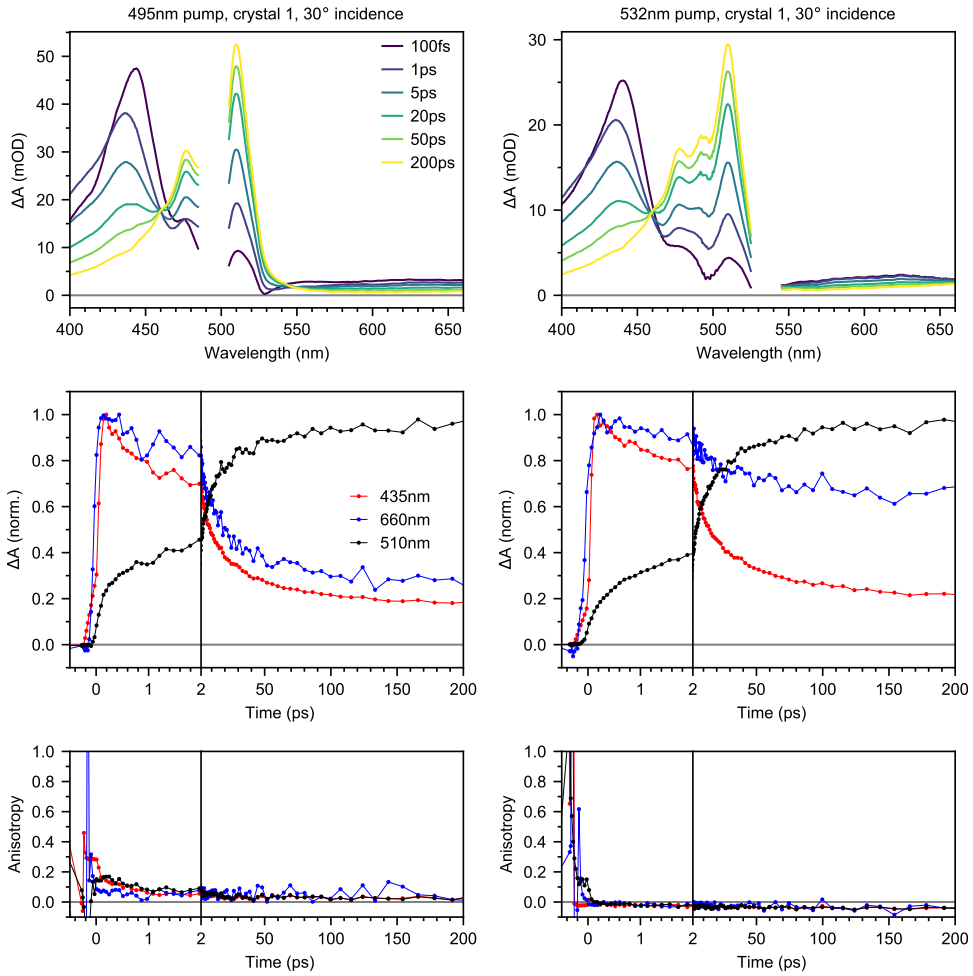

FIG. S12. **TA datasets for crystal 2, 30° incidence.** Transient absorption of crystal 2 at 30° incidence, excited with 495 nm and 532 nm pumps (left and right columns respectively). Spectra (top row) show a clear evolution from singlets ($S_1 \rightarrow S_3$ excited state absorption at 435 nm) to triplet-pairs ($T_1 \rightarrow T_3$ excited state absorption at 510 nm). The isosbestic point at 460 nm is slightly less pronounced than in crystal 1. The dynamics (middle row) and anisotropy (bottom row) are shown for probe wavelengths of 435 nm (mostly singlets, some triplets), 660 nm (mixture of singlets and triplets) and 510 nm (almost entirely triplets).

perpendicular, $\Delta A_\perp$. The isotropic signal, proportional to that measured at the magic angle, can then be recovered through [4]

$$\Delta A_{iso} = \Delta A_\parallel + 2\Delta A_\perp. \tag{2}$$

For crystal 1, the anisotropy is entirely independent of time, giving perfect agreement between $\Delta A_\parallel$ and ΔA_{iso} as shown in Figure S16a. For the polycrystalline film, the anisotropy

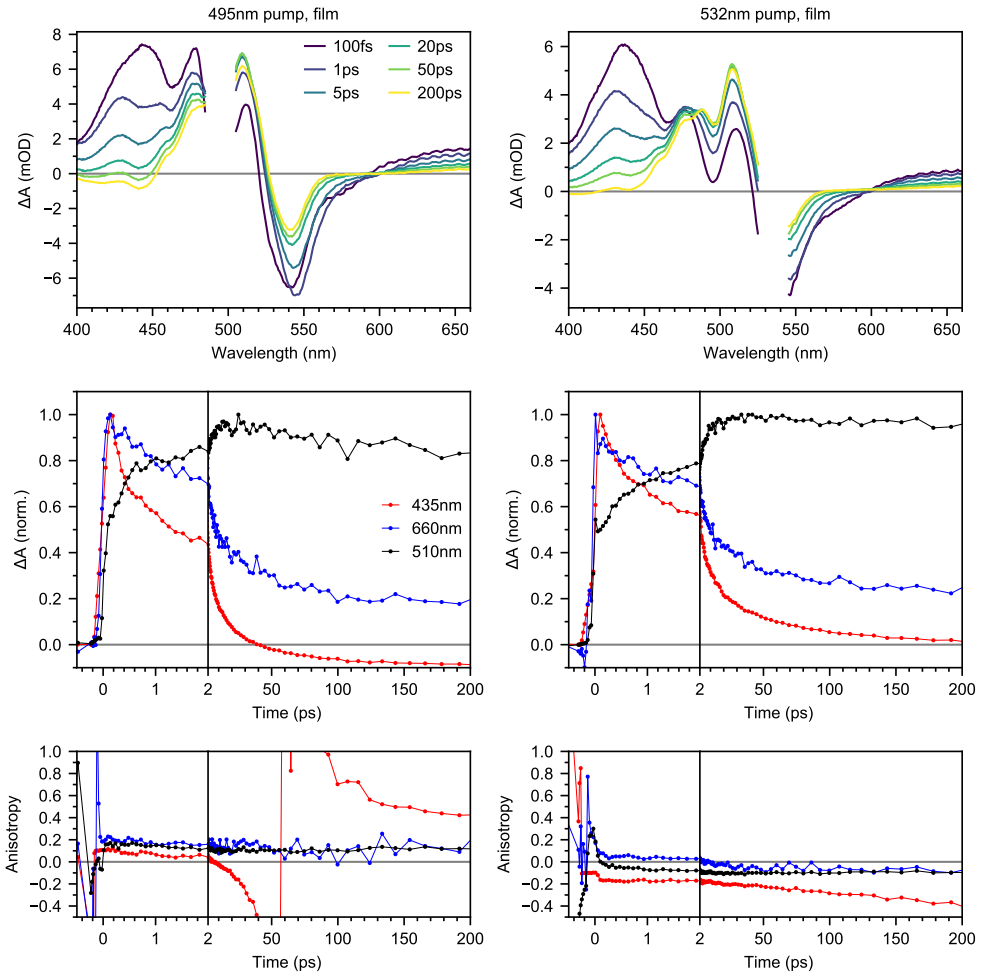

FIG. S13. **TA datasets for a polycrystalline film.** Transient absorption of the polycrystalline film at 0° incidence, excited with 495 nm and 532 nm pumps (left and right columns respectively). Spectra (top row) show a clear evolution from singlets ($S_1 \rightarrow S_3$ excited state absorption at 435 nm) to triplet-pairs ($T_1 \rightarrow T_3$ excited state absorption at 510 nm). The ground state bleach is much more pronounced than in the crystals. The dynamics (middle row) and anisotropy (bottom row) are shown for probe wavelengths of 435 nm (mostly singlets, some triplets), 660 nm (mixture of singlets and triplets) and 510 nm (almost entirely triplets). The anisotropy at 435 nm, for the 495 nm excitation diverges at around 50 ps because the signal crosses from positive to negative ΔA at that time.

exhibits a small time dependence, thus the agreement is not perfect. However, we note that all important features of the data, in particular the instrument-limited rise at 510 nm, are the same regardless of polarisation.

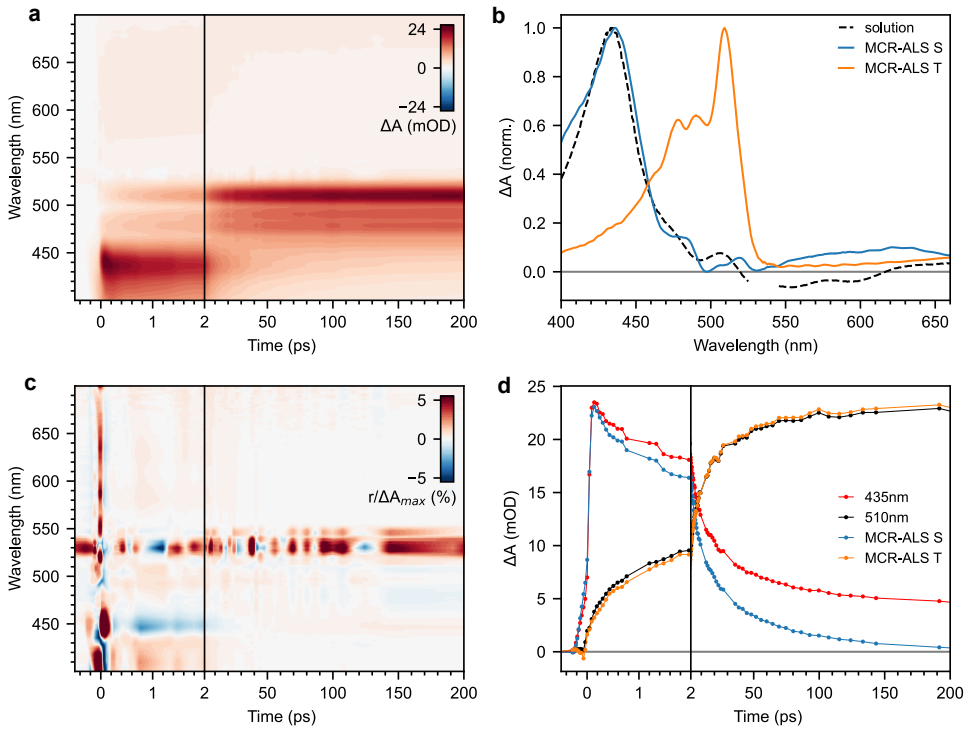

FIG. S14. **MCR-ALS of crystal 1 TA data.** **a**, Transient absorption spectroscopy of crystal 1 excited at 532 nm at 30° incidence. **b**, Singlet and triplet spectral components extracted via MCR-ALS. A spectrum measured for rubrene solution (10^{-4} M toluene), in which only singlets are present, is shown for comparison. **c**, Residuals between the data (**a**) and the MCR-ALS reconstruction, normalised to the maximum signal. The residuals are well below 5% except in the vicinity of the pump scatter and time-zero. **d**, Kinetics at probe wavelengths of 435 nm and 510 nm compared against the singlet and triplet population dynamics extracted via MCR-ALS.

[1] A. R. McGhie, A. F. Garito, and A. J. Heeger, A gradient sublimer for purification and crystal growth of organic donor and acceptor molecules, J. Cryst. Growth **22**, 295 (1974).

[2] O. D. Jurchescu, J. Baas, and T. T. M. Palstra, Effect of impurities on the mobility of single crystal pentacene, Appl. Phys. Lett. **84**, 3061 (2004).

[3] P. Irkhin, A. Ryasnyanskiy, M. Koehler, and I. Biaggio, Absorption and photoluminescence spectroscopy of rubrene single crystals, Phys. Rev. B **86**, 085143 (2012).

[4] E. J. Brown, I. Pastirk, and M. Dantus, Ultrafast rotational anisotropy measurements: Unidi-

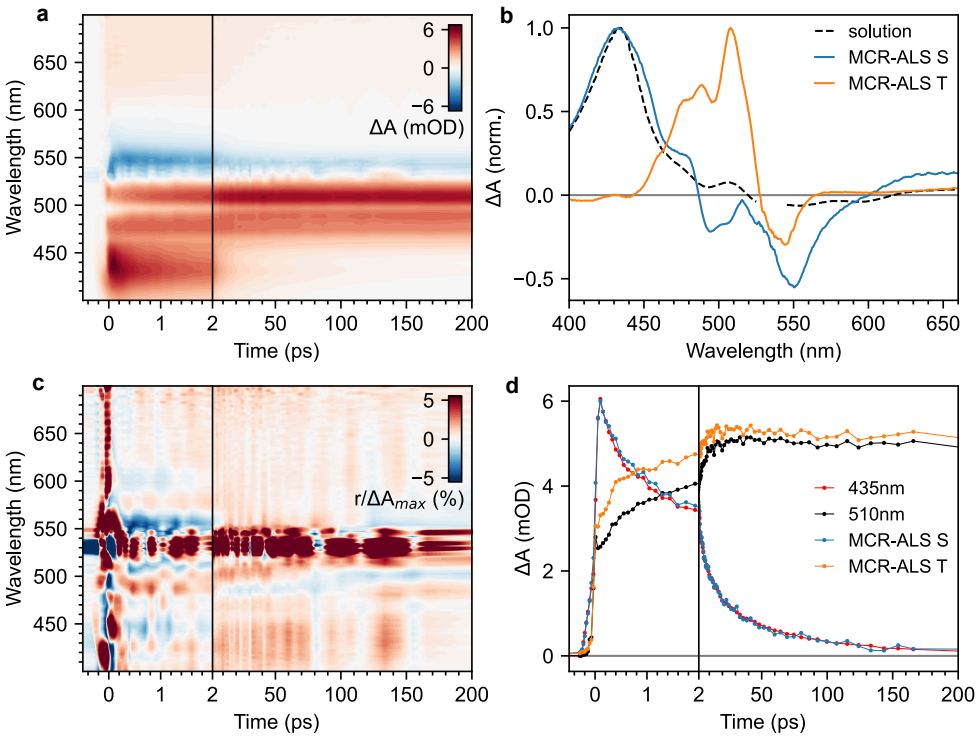

FIG. S15. **MCR-ALS of polycrystalline film TA data.** **a**, Transient absorption spectroscopy of a polycrystalline rubrene film excited at 532 nm. **b**, Singlet and triplet spectral components extracted via MCR-ALS. A spectrum measured for rubrene solution (10^{-4} M toluene), in which only singlets are present, is shown for comparison. **c**, Residuals between the data (**a**) and the MCR-ALS reconstruction, normalised to the maximum signal. The residuals are well below 5% except in the vicinity of the pump scatter and time-zero. **d**, Kinetics at probe wavelengths of 435 nm and 510 nm compared against the singlet and triplet population dynamics extracted via MCR-ALS.

rectional detection, J. Phys. Chem. A **103**, 2912 (1999).

[5] R. Berera, R. van Grondelle, and J. T. M. Kennis, Ultrafast transient absorption spectroscopy: principles and application to photosynthetic systems, Photosynth. Res. **101**, 105 (2009).

[6] J. Jaumot, R. Gargallo, A. de Juan, and R. Tauler, A graphical user-friendly interface for MCR-ALS: a new tool for multivariate curve resolution in MATLAB, Chemom. Intell. Lab. Syst. **76**, 101 (2005).

[7] J. Jaumot, A. de Juan, and R. Tauler, MCR-ALS GUI 2.0: New features and applications, Chemom. Intell. Lab. Syst. **140**, 1 (2015).

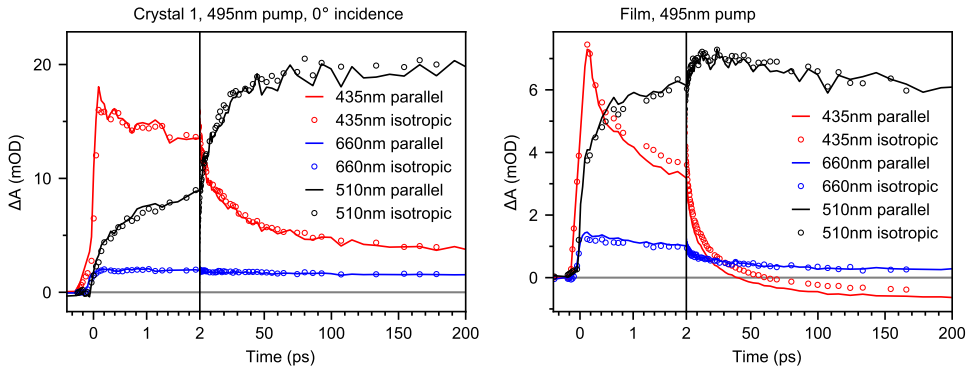

FIG. S16. **TA anisotropy.** **a**, TA kinetics for rubrene single crystal 1 excited at 495 nm at 0° incidence. Both the parallel and isotropic data are shown. The isotropic data have been scaled by a constant factor. **b**, As for (**a**), but for the polycrystalline film excited at 495 nm.